Canadian biomass burning aerosols observations from a multi-wavelength Raman polarization lidar and a ceilometer in Finland

Xiaoxia Shang[1], Tero Mielonen[1], Antti Lipponen[1], Elina Giannakaki[1,2], Ari Leskinen[1,3], Virginie Buchard[4,5], Anton S. Darmenov[4], Antti Kukkurainen[1,3], Antti Arola[1], Ewan O'Connor[6], Anne Hirsikko[6], Mika Komppula[1]

[1]Finnish Meteorological Institute, Kuopio, Finland
[2]Department of Environmental Physics and Meteorology, University of Athens, Athens, Greece
[3]Department of Applied Physics, University of Eastern Finland, Kuopio, Finland
[4]NASA/Goddard Space Flight Center, Greenbelt, MD, USA
[5]GESTAR/Universities Space Research Association, Columbia, MD, USA
[6]Finnish Meteorological Institute, Helsinki, Finland

Correspondence to: Xiaoxia Shang (xiaoxia.shang@fmi.fi)

Abstract. Layers of biomass burning aerosol particles were observed in the lower troposphere, at 2 to 5 km height on 4 to 6 June 2019, over Kuopio, Finland. These long-range-transported smoke particles originated from a Canadian wildfire event. The most pronounced smoke plume detected on 5 June was intensively investigated. Optical properties were retrieved from the multi-wavelength Raman polarization lidar Polly[XT]. Particle linear depolarization ratios of this plume were measured to be 0.08 ± 0.02 at 355 nm and 0.05 ± 0.01 at 532 nm which were slightly higher than the values given in the literature. Non-spherical shaped aged smoke particles and/or the mixing with a small amount of fine dust particles could cause the observed increase in the particle linear depolarization ratios. Lidar ratios were derived as 47 ± 5 sr at 355 nm and 71 ± 5 sr at 532 nm. A complete ceilometer data processing for a Vaisala CL51 is presented, including the water vapor correction for high latitude for the first time, from sensor provided attenuated backscatter coefficient to particle mass concentration. A combined lidar and sun-photometer approach (based on AERONET products) is applied for mass concentration estimations. Mass concentrations were estimated from both Polly[XT] and the ceilometer CL51 observations, which were of the order of ~ 30 μg m^{-3} in the morning and decreased to ~ 20 μg m^{-3} in the night. A difference of ~ 30 % was found between Polly[XT] and CL51 estimated mass concentrations. The mass retrievals were discussed and compared with the Modern-Era Retrospective analysis for Research and Applications, version 2 (MERRA-2) meteorological and aerosol reanalysis. The inclusion of dust in the retrieved mass concentration slightly improved the correspondence between the observations and the MERRA-2 simulations.

1 Introduction

Wildfires release large amounts of aerosols into the atmosphere, contributing significantly to direct radiative forcing (IPCC 2013, https://www.ipcc.ch/site/assets/uploads/2018/02/WG1AR5_Chapter08_FINAL.pdf, last access: 31 March 2021) and

affecting cloud optical properties by acting as cloud condensation nuclei (Yu, 2000) or ice nuclei (Prenni et al., 2012). Biomass burning is the dominant global source for carbonaceous aerosols, including organic and black carbon (Andreae, 2019), which can be transported over thousands of kilometres in the atmosphere (Andreae, 1991; Fromm and Servranckx,

35 2003; Mielonen et al., 2012; Portin et al., 2012). These smoke plumes can mix with other aerosols (such as dust) originating from regional and local sources (Osborne et al., 2019; Tesche et al., 2009). Long-range transport of particles originating from biomass burning has been recognized as a significant source of tropospheric aerosols at northern latitudes (Generoso et al., 2003), with the most common being smoke from Russia or North America (Müller et al., 2005; Wotawa et al., 2001). The optical properties of smoke particles vary depending on the vegetation fuel types in the source regions and the

40 combustion phase; they also change frequently when dispersing in the air (Reid et al., 2005a, 2005b).

Lidars provide quantitative range-resolved information of atmospheric aerosols. Multi-wavelength Raman lidar, together with its depolarization capability, provides comprehensive information on aerosol optical and microphysical properties (e.g. Müller et al., 1999), and allow the identification of the aerosol type using the intensive optical parameters (Groß et al., 2013; Illingworth et al., 2015). Ground-based lidar networks, such as EARLINET (European Aerosol Research Lidar Network,

45 https://www.earlinet.org, last access: 3 May 2021, Pappalardo et al., 2014) and PollyNET (Raman and polarization lidar network, http://picasso.tropos.de, last access: 3 May 2021, Baars et al., 2016), have continued to provide observations of clouds and aerosols over large spatial scales. However, the spatial resolution remains sparse, as advanced lidars are expensive.

Several national weather services have built up ceilometer networks for cloud monitoring (e.g., http://ceilometer.fmi.fi,

50 Hirsikko et al., 2014, E-Profile: https://e-profile.eu, last access: 21 April 2021) with unattended operation on a 24/7 basis. Information from the large number of ceilometers in these networks can fill the gaps between advanced lidar stations. Ceilometers are single-wavelength, eye-safe backscatter lidars, originally designed to determine cloud base heights. Studies (e.g., Wiegner and Geiß, 2012) show that ceilometers can also be used to retrieve the aerosol backscatter coefficient with high accuracy. However, the accuracy of the aerosol extinction coefficient retrieval is sensitive to the estimate of the

55 unknown lidar ratio (LR). Ceilometers typically operate in the near-infrared (1064 nm or 910 nm) but the lidar ratios for different aerosol types have usually been observed and reported only at 532 and 355 nm. Only recently have lidar ratios at 1064 nm have been measured by Raman lidar (Haarig et al., 2016).

Several studies have investigated the properties of smoke plumes transported from Canadian wildfires to Europe (Ansmann et al., 2018; Fiebig et al., 2003; Hu et al., 2019; Müller et al., 2005), showing that biomass burning aerosols are medium- to

60 high-absorbing particles with an almost spherical shape and small particle size, producing medium to high lidar ratios, low depolarization ratios and high Ångström exponents. For example, Haarig et al. (2018) report for western Canadian wildfire smoke in both tropospheric and stratospheric layers over Leipzig, lidar ratios of 40–45 sr (355 nm), 65–80 sr (532 nm), 80–95 sr (1064 nm), low depolarization ratio (<0.03 at 355, 532, 1064 nm) for plumes in the troposphere and higher depolarization ratio (0.22 at 355nm, 0.18 at 532 nm, 0.04 at 1064 nm) for plumes in the stratosphere.

65   Similar observational records over Northern Europe are more scarce in the literature. On 4–6 June 2019, biomass burning aerosol layers were observed in the lower troposphere over Kuopio, Finland. These smoke particles originated from a Canadian wildfire event. In this study, we present observations of the smoke plume from a multi-wavelength Raman polarization lidar Polly[XT] and a Vaisala CL51 ceilometer. A combined lidar–photometer approach is presented for estimating mass concentration as a good knowledge of the aerosol mass concentration is required from the aviation safety point of view

70   (Schumann et al., 2011). The potential for mass concentration retrieval from ceilometer observations is also discussed. This study reports, for the first time, the optical properties and the mass concentration estimations of Canadian wildfire smoke aerosols over Northern Europe, using both Raman lidar and ceilometer observations.

This paper is organized as follows: in Sect. 2, the measurement site, instrumentation, measurements and methods are described. In Sect. 3, the results are presented and discussed. The conclusions are given in Sect. 4.

75   2   Measurement site, instrumentation and data analysis

The Vehmasmäki station in Kuopio (62°44'N, 27°33'E; 190 m above sea level), belonging to the European Aerosol Research Lidar Network (EARLINET, https://www.earlinet.org, last access: 3 May 2021) and PollyNET (http://picasso.tropos.de, last access: 3 May 2021), is a rural site, located ~18 km from the city centre of Kuopio, in Eastern Finland. The station has been an operational profiling site since Autumn 2012 and is operated by the Finnish Meteorological Institute (Hirsikko et al.,

80   2014). It is equipped with a ground-based multi-wavelength Raman polarization lidar Polly[XT] (Baars et al., 2016; Engelmann et al., 2016), Vaisala ceilometers CL31 and CL51, a Doppler lidar, and in situ instruments, next to a 318 m tall mast (for the meteorological observations) during the period. Vehmasmäki is located far from major aerosol sources such as dust or anthropogenic aerosol and the atmosphere is relatively clean.

2.1   Ancillary data

85   The closest AErosol RObotic NETwork (AERONET, http://aeronet.gsfc.nasa.gov, last access: 3 May 2021) station to the Vehmasmäki site is the Kuopio station (62°53'N, 27°38'E; 105 m above sea level), ~18 km from Vehmasmäki. The AERONET sun-photometers measure the aerosol optical depth (AOD) from 340 to 1640 nm (eight channels) for the total atmospheric column, with an uncertainty from 0.01 to 0.02 (Eck et al., 1999). The AERONET (version 3.0) level 2.0 direct sun products (O'Neill, 2003) and inversion products (Dubovik and King, 2000) were used in this study. These products

90   include spectral AODs, fine-mode and coarse-mode AODs (at 440, 675, 870, 1020 nm of inversion products; or at 500 nm of direct sun products), fine-mode and coarse-mode related volume concentrations in the entire vertical atmospheric column. A detailed uncertainty analysis was performed by Dubovik et al. (2000), showing low errors in AOD, and about 10 %–20 % error in volume concentration.

Temperature   and   pressure   profiles   from   the   GDAS   (Global   Data   Assimilation   System,

95   https://www.ready.noaa.gov/gdas1.php, last access: 19 March 2021) database were used for the correction of Rayleigh

extinction and backscattering effects for lidar data analysis. HYSPLIT (Hybrid Single Particle Lagrangian Integrated Trajectory, https://ready.arl.noaa.gov/HYSPLIT.php, last access: 19 March 2021) backward trajectories were also analysed to study the air mass origins. Additionally, the thermal anomalies (fire sources) from Terra and Aqua MODIS data (MODIS, 2019) were synergistically used to locate where the forest fires were occurring.

100 Mass concentrations, absorption coefficients at 370–950 nm wavelengths, and scattering coefficients at 450–700 nm wavelengths of the aerosol at the ground level were measured with a Synchronized Hybrid Ambient Real-time Particulate Monitor (SHARP, Thermo Scientific, Model 5030), a seven-wavelength aethalometer (Magee Scientific, Model AE-31), and a three-wavelength nephelometer (TSI Inc., Model 3563), respectively. Particle size distribution was measured using a scanning mobility particle sizer (TSI Inc., Model 3910) and an optical particle sizer (TSI Inc., Model 3330), whose

105 measurements were combined in the size range of 10 nm–10 µm according to Alas et al. (2019). The particle mass concentrations and size distributions were used for monitoring the overall pollution level at the site, and the absorption and scattering coefficients were exploited in characterizing the aerosol optical properties in situ. The aethalometer and nephelometer data were corrected for the filter loading and multiple scattering artefacts, and the truncation artefact, respectively. The interpolations and extrapolations for matching the different wavelengths of the instruments were done by

110 using the Ångström exponent law. The contribution of other absorbing material than black carbon (BC), mainly brown carbon (BrC), to the absorption coefficients, was calculated from the corrected absorption coefficients at 370 and 880 nm by assuming an Ångström exponent of unity for BC. All corrections and data processing were performed in the same manner as described in Leskinen et al. (2020).

MERRA-2 is a global reanalysis produced with the NASA global Earth System model, GEOS (Goddard Earth Observing

115 System) coupled with the aerosol module GOCART (Goddard Chemistry, Aerosol, Radiation and Transport) (Gelaro et al., 2017) and includes the assimilation of aerosol observations (AOD) from various spaceborne instruments such as MODIS, AVHRR, MISR (Buchard et al., 2017; Randles et al., 2017). It has an approximate horizontal resolution of 0.5° × 0.625° and 72 hybrid-eta level levels from the surface to 0.01 hPa. Every 3 hours, MERRA-2 produces vertical profiles of aerosol mass mixing ratio for five aerosol species (dust, sea salt (SS), black and organic carbon (BC and OC), and sulfate (SU)) from

120 which lidar optical parameters, such as aerosol extinction and backscattering coefficients can be calculated.

2.2 Polly[XT] lidar

The multi-wavelength Raman polarization lidar Polly[XT] has three emission wavelengths (355, 532, 1064 nm) and 12 detection channels, including a far-range receiver unit with eight channels (355, 387, 407, 532, 607, 1064 nm, and two depolarization channels at 355 and 532 nm), a near-range receiver unit with four channels (355, 387, 532, and 607 nm). The

125 initial spatial and time resolution is 7.5 m and 30 s, respectively. The laser beams are tilted to an off-zenith angle of 5° to avoid specular reflections from horizontally aligned ice crystals.

Data processing methods of Raman lidars are well established. When the signal-to-noise ratio is high enough for the received signals at inelastic Raman-shifted wavelengths (387 and 607 nm), which is mainly during night-time, profiles of extinction

and backscatter coefficients at 355 and 532 nm can be derived independently using the Raman inversion technique
130 (Ansmann et al., 1992a). Otherwise, the Klett–Fernald method (Fernald, 1984; Klett, 1981) is applied using the elastic
signals to retrieve the backscatter coefficients. The overall relative uncertainties are in the range of 5–10 % for backscatter
coefficients and depolarization ratios, and 10–20 % for extinction coefficients (Ansmann et al., 1992b; Baars et al., 2012).
Further details on the instrument setup, principle and error propagation can be found in Engelmann et al. (2016).

2.3 Ceilometer and data processing

135 The Vaisala CL51 ceilometer used in this study is a commercial elastic backscatter lidar originally intended for measuring
cloud base heights. It operates at 910 nm with an initial temporal resolution of 10 s and range resolution of 10 m, and was
tilted to an angle of 12°–13° from vertical. The horizontal distances between the laser beams of CL51 and Polly^{XT} are of the
order of ~ 700 m at 5 km, which is considered negligible in this study. The signal-to-noise ratio (SNR) for raw CL51
backscatter signals above the boundary layers is weak, hence some temporal averaging and vertical smoothing were required
140 when performing further analysis.

Kotthaus et al. (2016) states that background corrections are needed for some ceilometer firmware versions. Following the
method proposed in Kotthaus et al. (2016), range histograms of observations from CL51 on clear-sky days were analysed.
The results show that the background corrections are not needed for the CL51 data from Kuopio station, because the CL51 is
operating with a specific firmware version which is recommended by E-Profile and ACTRIS (the Aerosol, Clouds and Trace
145 Gases Research Infrastructure, https://www.actris.eu, last access: 3 May 2021).

The instrument constant is not accurately calibrated in absolute terms for many of the ceilometers in the network
(http://ceilometer.fmi.fi, last access: 3 May 2021), because the main application is the cloud-base height detection in which a
correct instrument constant is not required. Different calibration procedures (e.g., relative/absolute calibration) have been
proposed and applied in literature. The stratocumulus cloud technique (O'Connor et al., 2004) is the most appropriate for the
150 CL51 sensor which was used in this study and recommended by E-Profile for this sensor type. Stratocumulus cloud cases in
2019 were analysed, and five good cases from April to September 2019 were found. A calibration factor of 1.75 ± 0.03 was
derived with small standard deviation during the 6 months, showing that the CL51 system is quite stable. A relative
uncertainty on the instrument constant within 10 % should be considered, as the calibration approach contains a range of
possible multiple-scattering factors.

155 Wiegner and Gasteiger (2015) report that the ceilometer signal must be corrected for water vapor if emitting wavelengths
around 910 nm are used. They show that the error in the backscatter coefficient retrieval can be in the order of 20 % for mid-
latitudes, and more than 50 % for the tropics, if water vapor absorption is ignored. We performed similar simulations in
Kuopio station, following the method given in Wiegner and Gasteiger (2015). The water vapor number densities were
calculated from the relative humidity and the temperature profiles from GDAS1 data. The water vapor absorption cross-
160 sections in the spectral range between 900 and 920 nm were simulated based on HITRAN (Rothman et al., 2005) data base,
which covers a wide range between 10^{-28} cm^2 and 10^{-21} cm^2. For the CL51, we assumed a Gaussian shape of the spectrum,

with the central wavelength of 910 nm and a full width at half maximum of 3.4 nm, as specified by Vaisala. Thus, the water vapor transmission can be estimated, and the effective water vapor transmission was applied to the ceilometer signals for the water vapor corrections (equations and more details can be found in Wiegner and Gasteiger, 2015). One example is given in

165 Fig. 1:

(I) Using the forward integration method, the retrieved particle backscatter coefficients without water vapor correction (β^*) were much lower than the ones with water vapor correction (β) (Fig. 1c). This underestimate increased with height in the boundary layer, and with ~ 40 % for the elevated layer.

(II) Using the backward integration method, neglecting the water vapor led to an overestimate, which increased

170 with the distance from the chosen reference height. An overestimate of ~ 50 % can be found at near ground for the given example. Nevertheless, a much smaller error (~ 6 %) was found for the elevated layer using this method compared to the forward integration method.

As the water vapor contribution cannot be neglected at Kuopio during summer, the water vapor corrections have been applied to CL51 data in this study.

175 The retrieval methods for deriving the backscatter coefficient from ceilometers are quite mature (Wiegner et al., 2014; Wiegner and Geiß, 2012); the relative error is less than 10 %. However, the accuracy in deriving extinction coefficients is limited due to the unknown LR at 910 or 1064 nm. In this study, we applied the Klett method (Wiegner et al., 2014) by defining the reference height just below the layer of interest, so that the error propagation would be minimized for that layer. Characteristic LR values for aerosol types are often measured at 355 or 532 nm; it is only recently that Haarig et al. (2016)

180 measured the LR at 1064 nm, and reported values of 80–95 sr for aged biomass burning smoke (Haarig et al., 2018). A value of 82 sr for LR, as measured at 1064 nm (Haarig et al., 2018), was assumed as being appropriate for use at 910 nm in this study.

3   Results and discussion

From 4 to 6 June 2019, several lofted aerosol particle layers were detected with Polly[XT] (near-real-time quick-looks are

185 publicly accessible at the PollyNET website: http://picasso.tropos.de, last access: 3 May 2021). The AERONET sun-photometer observed enhanced AOD values for these days: the total AOD at 500 nm ranged from 0.24 to 0.42, whereas the mean values for the previous week and the following week were both below 0.08.

In this study, we focus on the observations on 5 June, when the most pronounced aerosol layers were detected. Range-corrected signal (RCS) at 1064 nm from Polly[XT] and at 910 nm from CL51 on 5–6 June are presented in Fig. 2. A dense

190 lofted aerosol layer was highlighted by the enhanced lidar signals, located at ~ 5 km in the morning and which descended to ~ 2 km in the evening; this layer is defined as SPoI (Smoke Plume of Interest). Two faint lofted thin layers were also detected below this layer in the morning. The presence of pollen in the boundary layer (below 2 km) caused strong

backscattering together with high depolarization ratio at 532 nm with a clear diurnal cycle. Although also of interest, the analysis of the pollen layer is out of the scope of this paper.

195   As shown in Fig. 3, the AERONET fine-mode AOD fraction on 5 June was higher than 93 %, and the Ångström exponent at 500–870 nm (380–500 nm) varied between 1.4 and 1.7 (0.8 and 1.1), indicating the presence of fine particles in the atmospheric column. The coarse-mode AOD slightly increased during the daytime (always below 0.02) on 5 June, which can be interpreted as the pollen-related contribution to optical depth in the boundary layer. The higher coarse-mode AODs on 6 June could also be a consequence of higher pollen contributions. As a consequence, ceilometer signals were almost totally

200   attenuated above 3 km on 6 June (Fig. 2b).

The backward trajectory analysis was performed using the HYSPLIT model. The analysis shows that particles in the SPoI had travelled about seven days from the forest fire sources (MODIS, 2019) in western Canada to North Europe (Fig. 4).

An increase in the aerosol mass concentration and absorption and scattering coefficients at ground level was observed only after 6 June (Fig. 5). The values were noticeably higher than the long-term (2013–2020) median values at the site: 3.1 $\mu g\ m^{-3}$

205   for the mass concentration, 0.4 Mm^{-1} for the absorption coefficient at 880 nm, and 9.8, 6.2, 3.9, and 2.6 Mm^{-1} for the scattering coefficients at 450, 550, 700, and 880 nm, respectively. During the period with elevated mass concentration, the median size of the accumulation mode particles increased from about 100 nm to 120 nm and a higher concentration of supermicron particles was also observed. The concentrations stayed elevated for several days, which indicated a long-range-transport aerosol event rather than a local one, and which may have been connected to the aerosol layer observed first with

210   the lidars and later with the in situ instruments at the ground level and refer to the deposition of the aerosol particles to the ground. The increase in the absorption coefficient at 880 nm indicates a higher black carbon (BC) content in the aerosol, a combustion derived aerosol component that is found in, e.g., biomass burning or traffic emissions. The more intense increase in the absorption coefficient at 370 nm and an increase in the calculated BrC fraction indicates a higher fraction of aerosol of biomass burning origin.

215   **3.1 Optical properties**

The pronounced smoke layer, i.e. SPoI shown in black box in Fig. 2, had a layer depth of ~ 1.8 km in the early morning, and became much thinner when descending at night. The Polly^{XT}-derived AOD at 355 nm (532 nm) of this layer decreased from 0.21 (0.13) in the morning to 0.04 (0.02) in the night.

Layer-mean values of optical properties of the SPoI were derived and are given in Table 1. Two-hour time-averaged lidar

220   profiles were used in order to increase SNR. LR retrievals at 355 nm were available for the whole day, providing layer-mean values of 47 ± 5 sr which remained quite constant during the period. LR retrievals at 532 nm were only possible after sunset (after 18h UTC), resulting in layer-mean values of 71 ± 5 sr. The 532 nm lidar ratio for aged smoke is larger than the 355 nm lidar ratio, in contrast to urban haze and fresh smoke, where the 355 nm lidar ratio is typically larger than the 532 nm lidar ratio (e.g., Nicolae et al., 2013; Pereira et al., 2014). Actually, as stated by Ansmann et al. (2020) and references therein, this

225 characteristic ratio in LR, i.e. LR(355 nm) / LR(532 nm) <1, is not produced by any other aerosol type and allows a clear identification of aged smoke.

The backscatter coefficients of aged wildfire smoke show a clear and strong wavelength dependence for both 355–532 nm and 532–1064 nm wavelength ranges; the backscatter-related Ångström exponent between 355 and 532 nm (between 532 and 1064 nm) shows high values of ~ 2.5 (~ 2.2). Nonetheless, the wavelength dependence of the extinction coefficient for

230 the 355–532 nm spectral range is much weaker, with an extinction-related Ångström exponent of ~ 1.4. These high Ångström exponent values indicate that fine particles dominated the observed optical properties.

The smoke particles caused low particle linear depolarization ratios (PDR) at 355 nm (532 nm) with a mean value of 0.08 ± 0.02 (0.05 ± 0.01) in the smoke layer. The layer-mean PDR at 355 nm (532 nm) decreased during the day, from ~ 0.11 (0.06) in the morning to ~ 0.05 (0.04) in the evening. This may indicate that the large and/or non-spherical particles were deposited

235 more effectively than the small and/or spherical ones. The relative humidity (RH) profiles from GDAS1 data showed low values in the lower atmosphere (<60 % below 6 km) before 15h UTC, and even lower RH (<40 %) at the SPoI altitude. RH slightly increased in the evening. The signal in the 407 nm Raman-shifted channel was used to determine the water vapor mixing ratio profile during night-time, showing that the layer-mean RH changed from ~ 27 % at 19 h to ~ 38 % at 23 h, which was associated with the advection of a moister air mass with a water vapor mixing ratio close to 1–3 g kg^{-1}. The

240 smoke particles were dry, and then captured water vapor in the atmosphere during the evening. Compared to the depolarization ratio of biomass burning aerosols reported in the literature (Table 1), our study presented slightly higher PDR values, suggesting the presence of partly coated soot particles or particles that have mixed with a small amount of dust or other non-spherical aerosol type.

3.2 Mass concentration estimation

245 Ansmann et al., (2011) present a combined lidar-photometer method that enables the retrieval of the vertical profiles of ash and non-ash (fine-mode) particle mass concentration (m). It is based on the mass density (ρ) of considered particles (mainly from literature), the volume-to-extinction conversion factors c_v (from literature or computed from AERONET sun-photometer products), the backscatter coefficient (β) (from lidar measurements), and the lidar ratio (LR) (from Raman lidar measurements or assumptions depending on aerosol types), following the equation:

250 $$m_a = \rho_a \cdot c_{v,a}(\lambda) \cdot \beta_a(\lambda) \cdot LR_a(\lambda) \,, \tag{1}$$

where a indicates the aerosol type, and λ the wavelength. $c_{v,a}$ uses the temporal mean value within a given time period to convert particle extinction coefficients into particle volume concentrations:

$$c_{v,a}(\lambda) = \overline{\left(\frac{v_a}{\tau_a(\lambda)}\right)} \,. \tag{2}$$

The column particle volume concentration v and corresponding optical thickness τ for aerosol component a are obtained from AERONET sun-photometer products.

This approach was applied to both Polly^{XT} and CL51 data to estimate the mass concentration profiles for biomass burning aerosols in the SPoI.

3.2.1 Wildfire smoke aerosols

We first assume that there are only biomass burning aerosols in the SPoI. Values for the smoke particle density vary in the literature (Chen et al., 2017; Li et al., 2016; Reid et al., 2005a), but should be in the range of 1.0–1.3 g cm^{-3} (Ansmann et al., 2020). In this study, a particle density ρ_s of 1.3 g cm^{-3} was used for the biomass burning particles. Since AERONET inversion products of level 2.0 were not available on 5 June 2019, the AERONET products for the observations on 6 June 2019 (three distributions at 06:33, 07:10, and 14:41) were used to compute the volume-to-extinction conversion factors at different wavelengths for fine-mode particles ($c_{v,s}$). Here, the assumption is made that the photometer-derived fine particle are mainly smoke particles. Both the Dubovik approach (Dubovik et al., 2006; Dubovik and King, 2000) and the O'Neill method (2003) were applied at the wavelength of 532 nm, resulting in similar values for this factor (~ 0.1 % difference). For wavelengths of 355 nm and 910 nm, only the Dubovik approach was applied. The mean conversion factors at three wavelengths are given in Table 2 together with their standard deviations. The conversion factor value at 532 nm of 0.211 ± 0.003 ·10^{-6} m is in good agreement with the values for smoke (from 0.12 to 0.21 ·10^{-6} m) at several AERONET stations reported in Ansmann et al. (2020).

In the SPoI, the backscatter coefficient of smoke particles is assumed to be equal to the total backscatter coefficient ($\beta_s = \beta_{total}$). Figure 6 (a) shows the lidar-derived backscatter coefficients at 355 nm (blue), 532 nm (green), and 1064 nm (red) from Polly^{XT}, and at 910 nm (black) from CL51 for two-hour time-averaged lidar profiles on 5 June 2019. Signals were smoothed with vertical gliding averaging window lengths of 11 bins for Polly^{XT} and 7 bins for CL51. The peak value of backscatter coefficients in the SPoI reached ~ 5 Mm^{-1} sr^{-1} at 355 nm in the morning and reduced to ~ 3 Mm^{-1} sr^{-1} at 355 nm at night. These backscatter coefficients are converted to their respective extinction coefficients by multiplication with the smoke lidar ratios (Table 2). The estimated mass concentration profiles are given in Fig. 6 (b), based on the lidar-derived backscatter coefficient at 355, 532 or 910 nm, respectively. The peak mass concentrations reached values of ~ 45 µg m^{-3}. Good agreements are found between the mass concentrations estimated from the different wavelengths. If we take the mass concentration estimated from the backscatter coefficient at 532 nm (which is the wavelength most often used in earlier studies) as the reference, an underestimate of ~ 15 % (overestimate of ~ 30 %) was found when using backscatter coefficients at 355 nm (910 nm). The overestimate for CL51-derived mass concentrations could be due to an overestimate of LR at 910 nm, since we used LR at 1064 nm in the calculations.

The accuracy of the retrieved mass concentration depends on the accuracy of parameters (e.g., mass density and volume-to-extinction conversion factors) that are not derived from lidars and require information from additional instruments.

Especially when considering ceilometers, uncertainty in the lidar ratio will introduce additional uncertainties to the mass concentration estimates. The uncertainties in lidar and AERONET products were discussed in Sect. 2. If we assume typical uncertainties of 10 % in the backscatter coefficient, 20 % in the lidar ratio, 20 % in the volume-to-extinction conversion factor estimates, and 25 % in the mass density estimate (Ansmann et al., 2011), and apply the law of error propagation to Eq.

290 (1), we expect an uncertainty in the mass concentration estimate of about 40 %.

3.2.2 Wildfire smoke and dust aerosol mixture

The total mass concentrations from MERRA-2 model data are shown in Fig. 6 (b) for comparison. Good consistencies are found for mass concentrations in the morning and at night; whereas mass concentrations from MERRA-2 were higher than the lidar estimates in the afternoon.

295 MERRA-2 simulations show the presence of dust in the SPoI. The contribution of dust to the total AOD is very low (much lower than the carbon optical depth), indicating that the dust particles are in the fine mode. However, the dust contribution to the total mass concentration is non-negligible. Low values of lidar-derived depolarization ratio suggest no significant presence of non-spherical particles, but a small amount of dust could be mixed with the smoke as discussed in Sect. 3.1. It is possible that there are biomass burning aerosols and fine dust aerosols in the SPoI, as only fine dust particles should be able

300 to remain long enough in the atmosphere to be transported from North America to Kuopio.

The POLIPHON (Polarization lidar photometer networking) method (Mamouri and Ansmann, 2014, 2017) was applied to separate fine dust and biomass burning aerosols for the SPoI. Here we used the Polly^{XT} retrieved particle backscatter coefficient and particle linear depolarization ratio profiles at 532 nm, because the uncertainty in the 355 nm particle depolarization ratios are much larger (Mamouri and Ansmann, 2017). The depolarization ratios at 532 nm of smoke and fine

305 dust particles were assumed to be 0.03 (Haarig et al., 2018) and 0.16 (Sakai et al., 2010). The fine dust and smoke extinction coefficients were obtained by multiplying the backscatter coefficients with their respective lidar ratios as follows: Ansmann et al. (2019) report that the typical dust lidar ratio is 40 sr at 532 nm, and lidar ratios for fine- and coarse-mode dust were assumed to be the same. For smoke particles, we took the lidar ratio of 71 sr, which was retrieved during our nighttime measurements. The fine dust and smoke particle mass concentrations can be derived using Eq. (1), with conversion factors

310 c_v of 0.22 10^{-6} m (Ansmann et al., 2019) and 0.21 10^{-6} m, and particle densities of 2.6 g cm^{-3} (Ansmann et al., 2012) and 1.3 g cm^{-3} (Ansmann et al., 2020; Reid et al., 2005a), for fine dust and smoke, respectively. These parameters are reported in Table 3. For the example given in Fig. 7, the fine dust contributes ~ 13 % to the extinction in the SPoI, whereas its mass concentration contributes ~ 24 % to the total mass concentration. However, the derived total mass concentration considering a fine dust and smoke mixture is only ~ 4 % higher than one assuming smoke particles only. Estimated mass concentrations

315 of the SPoI under both assumptions are given in Fig. 6 (c). Overall, the mass concentration increased by ~ 3 % when considering a dust mixture for daytime estimates. The differences were even smaller for night-time estimates. This bias should be included in the uncertainty for the mass concentration estimate. The inclusion of a dust mixture slightly improved the agreement between the lidar-retrieved and model-simulated mass concentrations. It is good to keep in mind that both

observations and simulations have significant uncertainties. Large discrepancies were found for mass concentration estimates
320 in the afternoon, when the MERRA-2 simulated dust mass concentration fraction is more than half of the MERRA-2
simulated total mass concentration. The presence of depolarizing pollen particles in the boundary layer may have been
mistaken as dust particles in the model, contributing to large mass concentrations. The presence of cirrus cloud in the upper
atmosphere during the day may also have some impacts on MODIS AOD, which is assimilated by the MERRA-2 model.

It is not possible to perform the aerosol separation using ceilometer data alone, as no depolarization information is available
325 at this wavelength. For this instrument, only one aerosol type should always be assumed in the layer of interest, which then
imparts an additional bias when estimating the mass concentration. Uncertainties in the lidar ratio at ceilometer wavelengths
are much larger, compared to Raman lidars, which also results in higher uncertainties. Similar to the uncertainty calculation
described in Sect. 3.2.1, if we assume the ceilometer lidar ratio has an uncertainty of 50 % (instead of 20 % for Polly^{XT}), the
uncertainty in the mass concentration is about 63 % by the law of error propagation. Nevertheless, the good agreement
330 between mass concentrations derived from Polly^{XT} and CL51 measurements in this study show the potential of mass
concentration estimates from ceilometer. However, when deriving parameters such as mass concentration from ceilometer,
the applied parameters (e.g., LR value) and their uncertainty should always be carefully evaluated and provided, as the
accuracy of the retrieved mass concentration primarily depends on the accuracy of parameters that are not derived from the
ceilometer observations.

335 4   Summary and conclusions

On 4–6 June 2019, aerosol layers arising from biomass burning were observed in the lower troposphere between 2–5 km in
altitude over Kuopio, Finland. Enhanced backscattered signals were detected by both a multi-wavelength Raman polarization
lidar Polly^{XT} and a Vaisala CL51 ceilometer. The HYSPLIT backward trajectories analysis and MODIS fire data suggested
that these long-range-transported smoke particles originated from a Canadian wildfire event. An AERONET sun-photometer
340 located in Kuopio observed enhanced AOD values in concert with high Ångström exponents, indicating the presence of fine-
mode dominant aerosols in the atmospheric column. An increase in the aerosol mass concentration and absorption and
scattering coefficients at the ground level was observed only after 6 June, after the deposition of the aerosol particles from
this layer to the ground. The in situ measurements demonstrated a high black carbon content and an increase in the brown
carbon fraction, indicating aerosol of biomass burning origin.

345 The most pronounced smoke plume, defined as SPoI (Smoke Plume of Interest), detected on 5 June was intensively
investigated. Lidar ratios were derived from the Raman lidar, as 47 ± 5 sr at 355 nm and 71 ± 5 sr at 532 nm, showing that
the aerosols of biomass burning origin in the SPoI were medium- to high- absorbing particles. Particle linear depolarization
ratios in this layer were measured as 0.08 ± 0.02 at 355 nm and 0.05 ± 0.01 at 532 nm; which are slightly higher than values
given in the literature and which could indicate the presence of irregular-shaped aged smoke particles and/or mixing with a
350 small amount of fine dust particles. Complete processing steps for Vaisala CL51 ceilometer data analysis were firstly

reported in this study. The water vapor correction was analysed and applied at a high latitude for the first time, showing that water vapor absorption cannot be neglected for high latitude stations during summer. A combined lidar and sun-photometer approach (based on AERONET products) was applied to both Polly[XT] and CL51 data for estimating mass concentrations, resulting in good agreement. The retrieved mass concentration profiles were compared with MERRA-2 aerosol profiles.

355   Mass concentrations were estimated to be in the order of ~ 30 µm m^{-3} in the morning, and which decreased to ~ 20 µm m^{-3} towards the night. We considered and analysed two scenarios in the SPoI – 1) only smoke particles and 2) mixture of fine dust and smoke aerosols, and reported with the corresponding uncertainties. The inclusion of dust in the retrieved mass concentration slightly improved the agreement between the observations and the MERRA-2 simulations, although large discrepancies still remained for the afternoon cases. We demonstrated the potential of the Vaisala CL51 ceilometer to

360   contribute to atmospheric aerosol research in the vertical profile, from sensor-provided attenuated backscatter coefficient to particle mass concentration.

Data availability. The data for this paper are available from the authors upon request. Polly[XT] data quick-looks are available on the PollyNET website (http://polly.tropos.de, last access: 3 May 2021). Ceilometer quick-looks are available on FMI

365   Real-time ceilometer data (http://ceilometer.fmi.fi, last access: 3 May 2021) and data files on request from FMI data archive. Trajectories are calculated with the NOAA (National Oceanic and Atmospheric Administration) HYSPLIT (HYbrid Single-Particle Lagrangian Integrated Trajectory) model (https://ready.arl.noaa.gov/HYSPLIT.php, last access: 19 March 2021). Fire data are available at the NASA Worldview application (https://worldview.earthdata.nasa.gov, last access: 2 February 2021). MERRA-2 data are available through the NASA Goddard Earth Sciences (GES) Data and Information Services

370   Center (DISC) (https://disc.gsfc.nasa.gov/datasets?project=MERRA-2, last access: 16 April 2021). The AERONET (AErosol RObotic NETwork) data are available at http://aeronet.gsfc.nasa.gov (last access: 3 May 2021).

Author contributions. XS analysed the data and wrote the manuscript with contributions from co-authors. XS, TM, AL, AH, and MK conceptualized the study. EG and AA helped in the validation of lidar and AERONET data analysis. AL provided

375   and assured the quality of the in situ measurements. VB and AD provided and assured the quality of the MERRA-2 data. AK carried out the simulations for the water vapor absorption cross-sections. MK and EO run the lidars and collected the observational data. EO and AH helped in ceilometer data analysis. All authors were involved in the interpretation of the results, reviewing and editing the manuscript.

380   *Competing interests.* The authors declare that they have no conflict of interest.

Acknowledgements. The authors acknowledge the use of imagery from the NASA Worldview application (https://worldview.earthdata.nasa.gov, last access: 3 May 2021), part of the NASA Earth Observing System Data and Information System (EOSDIS). We thank the NOAA Air Resources Laboratory (ARL) for the provision of the HYSPLIT

385 transport and dispersion model used in this publication. The authors acknowledge the MODIS Science, Processing and Data Support Teams for producing and providing MODIS data. The authors thank Stephanie Bohlmann and Anu-Maija Sundström for fruitful discussions. Tero Mielonen's work was supported by the Academy of Finland (grant No. 30829).

Financial support. This research has been supported by the National Emergency Supply Agency (decision number 19078).

390 **References**

Alas, H. D. C., Weinhold, K., Costabile, F., Di Ianni, A., Müller, T., Pfeifer, S., Di Liberto, L., Turner, J. R. and Wiedensohler, A.: Methodology for high-quality mobile measurement with focus on black carbon and particle mass concentrations, Atmos. Meas. Tech., 12(9), 4697–4712, doi:10.5194/amt-12-4697-2019, 2019.

Ancellet, G., Pelon, J., Totems, J., Chazette, P., Bazureau, A., Sicard, M., Di Iorio, T., Dulac, F. and Mallet, M.: Long-range
395 transport and mixing of aerosol sources during the 2013 North American biomass burning episode: Analysis of multiple lidar observations in the western Mediterranean basin, Atmos. Chem. Phys., 16(7), 4725–4742, doi:10.5194/acp-16-4725-2016, 2016.

Andreae, M. O.: Biomass burning: Its history, use and distribution and its impact on environmental quality and global climate, in Global Biomass Burning: Atmospheric, Climatic and Biospheric Implications, edited by J. S. Levine, pp. 3–21,
400 MIT Press, Cambridge, Mass., 1991.

Andreae, M. O.: Emission of trace gases and aerosols from biomass burning - An updated assessment, Atmos. Chem. Phys., 19(13), 8523–8546, doi:10.5194/acp-19-8523-2019, 2019.

Ansmann, A., Wandinger, U., Riebesell, M., Weitkamp, C. and Michaelis, W.: Independent measurement of extinction and backscatter profiles in cirrus clouds by using a combined Raman elastic-backscatter lidar., Appl. Opt., 31(33), 7113,
405 doi:10.1364/AO.31.007113, 1992a.

Ansmann, A., Wandinger, U., Riebesell, M., Weitkamp, C. and Michaelis, W.: Independent measurement of extinction and backscatter profiles in cirrus clouds by using a combined Raman elastic-backscatter lidar, Appl. Opt., 31, 7113–7131, 1992b.

Ansmann, A., Tesche, M., Seifert, P., Groß, S., Freudenthaler, V., Apituley, A., Wilson, K. M., Serikov, I., Linné, H., Heinold, B., Hiebsch, A., Schnell, F., Schmidt, J., Mattis, I., Wandinger, U. and Wiegner, M.: Ash and fine-mode particle
410 mass profiles from EARLINET-AERONET observations over central Europe after the eruptions of the Eyjafjallajökull volcano in 2010, J. Geophys. Res., 116(12), D00U02, doi:10.1029/2010JD015567, 2011.

Ansmann, A., Seifert, P., Tesche, M. and Wandinger, U.: Profiling of fine and coarse particle mass: case studies of Saharan dust and Eyjafjallajökull/Grimsvötn volcanic plumes, Atmos. Chem. Phys., 12(20), 9399–9415, doi:10.5194/acp-12-9399-2012, 2012.

415 Ansmann, A., Baars, H., Chudnovsky, A., Mattis, I., Veselovskii, I., Haarig, M., Seifert, P., Engelmann, R. and Wandinger, U.: Extreme levels of Canadian wildfire smoke in the stratosphere over central Europe on 21-22 August 2017, Atmos. Chem.

Phys., 18(16), 11831–11845, doi:10.5194/acp-18-11831-2018, 2018.

Ansmann, A., Mamouri, R. E., Hofer, J., Baars, H., Althausen, D. and Abdullaev, S. F.: Dust mass, cloud condensation nuclei, and ice-nucleating particle profiling with polarization lidar: Updated POLIPHON conversion factors from global
420 AERONET analysis, Atmos. Meas. Tech., 12(9), 4849–4865, doi:10.5194/amt-12-4849-2019, 2019.

Ansmann, A., Ohneiser, K., Mamouri, R.-E., Knopf, D., Veselovskii, I., Baars, H., Engelmann, R., Foth, A., Jimenez, C., Seifert, P. and Barja, B.: Tropospheric and stratospheric wildfire smoke profiling with lidar: Mass, surface area, CCN and INP retrieval, Atmos. Chem. Phys. Discuss., 1–45, doi:10.5194/acp-2020-1093, 2020.

Baars, H., Ansmann, A., Althausen, D., Engelmann, R., Heese, B., Müller, D., Artaxo, P., Paixao, M., Pauliquevis, T. and
425 Souza, R.: Aerosol profiling with lidar in the Amazon Basin during the wet and dry season, J. Geophys. Res. Atmos., 117, D21201, doi:10.1029/2012JD018338, 2012.

Baars, H., Kanitz, T., Engelmann, R., Althausen, D., Heese, B., Komppula, M., Preißler, J., Tesche, M., Ansmann, A., Wandinger, U., Lim, J.-H., Ahn, J. Y., Stachlewska, I. S., Amiridis, V., Marinou, E., Seifert, P., Hofer, J., Skupin, A., Schneider, F., Bohlmann, S., Foth, A., Bley, S., Pfüller, A., Giannakaki, E., Lihavainen, H., Viisanen, Y., Hooda, R. K.,
430 Pereira, S. N., Bortoli, D., Wagner, F., Mattis, I., Janicka, L., Markowicz, K. M., Achtert, P., Artaxo, P., Pauliquevis, T., Souza, R. A. F., Sharma, V. P., van Zyl, P. G., Beukes, J. P., Sun, J., Rohwer, E. G., Deng, R., Mamouri, R.-E. and Zamorano, F.: An overview of the first decade of PollyNET: an emerging network of automated Raman-polarization lidars for continuous aerosol profiling, Atmos. Chem. Phys., 16(8), 5111–5137, doi:10.5194/acp-16-5111-2016, 2016.

Buchard, V., Randles, C. A., da Silva, A. M., Darmenov, A., Colarco, P. R., Govindaraju, R., Ferrare, R., Hair, J.,
435 Beyersdorf, A. J., Ziemba, L. D. and Yu, H.: The MERRA-2 aerosol reanalysis, 1980 onward. Part II: Evaluation and case studies, J. Clim., 30(17), 6851–6872, doi:10.1175/JCLI-D-16-0613.1, 2017.

Chen, J., Li, C., Ristovski, Z., Milic, A., Gu, Y., Islam, M. S., Wang, S., Hao, J., Zhang, H., He, C., Guo, H., Fu, H., Miljevic, B., Morawska, L., Thai, P., LAM, Y. F., Pereira, G., Ding, A., Huang, X. and Dumka, U. C.: A review of biomass burning: Emissions and impacts on air quality, health and climate in China, Sci. Total Environ., 579, 1000–1034,
440 doi:10.1016/j.scitotenv.2016.11.025, 2017.

Dubovik, O. and King, M. D.: A flexible inversion algorithm for retrieval of aerosol optical properties from Sun and sky radiance measurements, J. Geophys. Res. Atmos., 105(D16), 20673–20696, doi:10.1029/2000JD900282, 2000.

Dubovik, O., Smirnov, A., Holben, B. N., King, M. D., Kaufman, Y. J., Eck, T. F. and Slutsker, I.: Accuracy assessments of aerosol optical properties retrieved from Aerosol Robotic Network (AERONET) Sun and sky radiance measurements, J.
445 Geophys. Res. Atmos., 105(D8), 9791–9806, doi:10.1029/2000JD900040, 2000.

Dubovik, O., Sinyuk, A., Lapyonok, T., Holben, B. N., Mishchenko, M., Yang, P., Eck, T. F., Volten, H., Muñoz, O., Veihelmann, B., van der Zande, W. J., Leon, J.-F., Sorokin, M. and Slutsker, I.: Application of spheroid models to account for aerosol particle nonsphericity in remote sensing of desert dust, J. Geophys. Res., 111(D11), D11208, doi:10.1029/2005JD006619, 2006.

450 Eck, T. F., Holben, B. N., Reid, J. S., Dubovik, O., Smirnov, A., O'Neill, N. T., Slutsker, I. and Kinne, S.: Wavelength

dependence of the optical depth of biomass burning, urban, and desert dust aerosols, J. Geophys. Res. Atmos., 104(D24), 31333–31349, doi:10.1029/1999JD900923, 1999.

Engelmann, R., Kanitz, T., Baars, H., Heese, B., Althausen, D., Skupin, A., Wandinger, U., Komppula, M., Stachlewska, I. S., Amiridis, V., Marinou, E., Mattis, I., Linné, H. and Ansmann, A.: The automated multiwavelength Raman polarization
455 and water-vapor lidar PollyXT: the neXT generation, Atmos. Meas. Tech., 9(4), 1767–1784, doi:10.5194/amt-9-1767-2016, 2016.

Fernald, F. G.: Analysis of atmospheric lidar observations: some comments, Appl. Opt., 23, 652–653, 1984.

Fiebig, M., Stohl, A., Wendisch, M., Eckhardt, S. and Petzold, A.: Dependence of solar radiative forcing of forest fire aerosol on ageing and state of mixture, Atmos. Chem. Phys., 3(3), 881–891, doi:10.5194/acp-3-881-2003, 2003.

460 Fromm, M. D. and Servranckx, R.: Transport of forest fire smoke above the tropopause by supercell convection, Geophys. Res. Lett., 30(10), 1542, doi:10.1029/2002GL016820, 2003.

Gelaro, R., McCarty, W., Suárez, M. J., Todling, R., Molod, A., Takacs, L., Randles, C. A., Darmenov, A., Bosilovich, M. G., Reichle, R., Wargan, K., Coy, L., Cullather, R., Draper, C., Akella, S., Buchard, V., Conaty, A., da Silva, A. M., Gu, W., Kim, G. K., Koster, R., Lucchesi, R., Merkova, D., Nielsen, J. E., Partyka, G., Pawson, S., Putman, W., Rienecker, M.,
465 Schubert, S. D., Sienkiewicz, M. and Zhao, B.: The modern-era retrospective analysis for research and applications, version 2 (MERRA-2), J. Clim., 30(14), 5419–5454, doi:10.1175/JCLI-D-16-0758.1, 2017.

Generoso, S., Bréon, F. M., Balkanski, Y., Boucher, O. and Schulz, M.: Improving the seasonal cycle and interannual variations of biomass burning aerosol sources, Atmos. Chem. Phys., 3(4), 1211–1222, doi:10.5194/acp-3-1211-2003, 2003.

Groß, S., Esselborn, M., Weinzierl, B., Wirth, M., Fix, A. and Petzold, A.: Aerosol classification by airborne high spectral
470 resolution lidar observations, Atmos. Chem. Phys., 13(5), 2487–2505, doi:10.5194/acp-13-2487-2013, 2013.

Haarig, M., Engelmann, R., Ansmann, A., Veselovskii, I., Whiteman, D. N. and Althausen, D.: 1064nm rotational Raman lidar for particle extinction and lidar-ratio profiling: Cirrus case study, Atmos. Meas. Tech., 9(9), 4269–4278, doi:10.5194/amt-9-4269-2016, 2016.

Haarig, M., Ansmann, A., Baars, H., Jimenez, C., Veselovskii, I., Engelmann, R. and Althausen, D.: Depolarization and lidar
475 ratios at 355, 532, and 1064 nm and microphysical properties of aged tropospheric and stratospheric Canadian wildfire smoke, Atmos. Chem. Phys., 18(16), 11847–11861, doi:10.5194/acp-18-11847-2018, 2018.

Hirsikko, A., O'Connor, E. J., Komppula, M., Korhonen, K., Pfüller, A., Giannakaki, E., Wood, C. R., Bauer-Pfundstein, M., Poikonen, A., Karppinen, T., Lonka, H., Kurri, M., Heinonen, J., Moisseev, D., Asmi, E., Aaltonen, V., Nordbo, A., Rodriguez, E., Lihavainen, H., Laaksonen, A., Lehtinen, K. E. J., Laurila, T., Petäjä, T., Kulmala, M. and Viisanen, Y.:
480 Observing wind, aerosol particles, cloud and precipitation: Finland's new ground-based remote-sensing network, Atmos. Meas. Tech., 7(5), 1351–1375, doi:10.5194/amt-7-1351-2014, 2014.

Hu, Q., Goloub, P., Veselovskii, I., Bravo-Aranda, J. A., Elisabeta Popovici, I., Podvin, T., Haeffelin, M., Lopatin, A., Dubovik, O., Pietras, C., Huang, X., Torres, B. and Chen, C.: Long-range-transported Canadian smoke plumes in the lower stratosphere over northern France, Atmos. Chem. Phys., 19(2), 1173–1193, doi:10.5194/acp-19-1173-2019, 2019.

485 Illingworth, A. J., Barker, H. W., Beljaars, A., Ceccaldi, M., Chepfer, H., Clerbaux, N., Cole, J., Delanoë, J., Domenech, C., Donovan, D. P., Fukuda, S., Hirakata, M., Hogan, R. J., Huenerbein, A., Kollias, P., Kubota, T., Nakajima, T., Nakajima, T. Y., Nishizawa, T., Ohno, Y., Okamoto, H., Oki, R., Sato, K., Satoh, M., Shephard, M. W., Velázquez-Blázquez, A., Wandinger, U., Wehr, T. and van Zadelhoff, G.-J.: The EarthCARE Satellite: The Next Step Forward in Global Measurements of Clouds, Aerosols, Precipitation, and Radiation, Bull. Amer. Meteor. Soc., 96, 1311–1332,
490 doi:10.1175/BAMS-D-12-00227.1, 2015.

Janicka, L., Stachlewska, I. S., Veselovskii, I. and Baars, H.: Temporal variations in optical and microphysical properties of mineral dust and biomass burning aerosol derived from daytime Raman lidar observations over Warsaw, Poland, Atmos. Environ., 169, 162–174, doi:10.1016/j.atmosenv.2017.09.022, 2017.

Klett, J. D.: Stable analytical solution for processing lidar returns, Appl. Opt., 20, 211–220, 1981.

495 Kotthaus, S., O'Connor, E., Münkel, C., Charlton-Perez, C., Haeffelin, M., Gabey, A. M. and Grimmond, C. S. B.: Recommendations for processing atmospheric attenuated backscatter profiles from Vaisala CL31 ceilometers, Atmos. Meas. Tech., 9(8), 3769–3791, doi:10.5194/amt-9-3769-2016, 2016.

Leskinen, A., Ruuskanen, A., Kolmonen, P., Zhao, Y., Fang, D., Wang, Q., Gu, C., Jokiniemi, J., Hirvonen, M.-R., Lehtinen, K. E. J., Romakkaniemi, S. and Komppula, M.: The Contribution of Black Carbon and Non-BC Absorbers on Aerosol
500 Absorption Coefficient in Nanjing, China, Aerosol Air Qual. Res., 20(3), 590–605, doi:10.4209/aaqr.2019.06.0326, 2020.

Li, C., Hu, Y., Chen, J., Ma, Z., Ye, X., Yang, X., Wang, L., Wang, X. and Mellouki, A.: Physiochemical properties of carbonaceous aerosol from agricultural residue burning: Density, volatility, and hygroscopicity, Atmos. Environ., 140, 94–105, doi:10.1016/j.atmosenv.2016.05.052, 2016.

Mamouri, R. E. and Ansmann, A.: Fine and coarse dust separation with polarization lidar, Atmos. Meas. Tech., 7(11), 3717–
505 3735, doi:10.5194/amt-7-3717-2014, 2014.

Mamouri, R. E. and Ansmann, A.: Potential of polarization/Raman lidar to separate fine dust, coarse dust, maritime, and anthropogenic aerosol profiles, Atmos. Meas. Tech., 10(9), 3403–3427, doi:10.5194/amt-10-3403-2017, 2017.

Mielonen, T., Portin, H., Komppula, M., Leskinen, A., Tamminen, J., Ialongo, I., Hakkarainen, J., Lehtinen, K. E. J. and Arola, A.: Biomass burning aerosols observed in Eastern Finland during the Russian wildfires in summer 2010 - Part 2:
510 Remote sensing, Atmos. Environ., 47, 279–287, doi:10.1016/j.atmosenv.2011.07.016, 2012.

MODIS: MODIS Collection 6 NRT Hotspot / Active Fire Detections MCD14DL. Available on-line [https://earthdata.nasa.gov/firms]. doi: 10.5067/FIRMS/MODIS/MCD14DL.NRT.006, 2019.

Müller, D., Wandinger, U. and Ansmann, A.: Microphysical particle parameters from extinction and backscatter lidar data by inversion with regularization: theory, Appl. Opt., 38(12), 2346–2357, doi:10.1364/AO.38.002346, 1999.

515 Müller, D., Mattis, I., Wandinger, U., Ansmann, A., Althausen, D. and Stohl, A.: Raman lidar observations of aged Siberian and Canadian forest fire smoke in the free troposphere over Germany in 2003: Microphysical particle characterization, J. Geophys. Res., 110, D17201, doi:10.1029/2004JD005756, 2005.

Müller, D., Ansmann, A., Mattis, I., Tesche, M., Wandinger, U., Althausen, D. and Pisani, G.: Aerosol--type--dependent

lidar ratios observed with Raman lidar, J. Geophys. Res. Atmos., 112, D16202, doi:10.1029/2006JD008292, 2007.

520 Nicolae, D., Nemuc, A., Müller, D., Talianu, C., Vasilescu, J., Belegante, L. and Kolgotin, A.: Characterization of fresh and aged biomass burning events using multiwavelength Raman lidar and mass spectrometry, J. Geophys. Res. Atmos., 118(7), 2956–2965, doi:10.1002/jgrd.50324, 2013.

O'Connor, E. J., Illingworth, A. J. and Hogan, R. J.: A technique for autocalibration of cloud lidar, J. Atmos. Ocean. Technol., 21(5), 777–786, doi:10.1175/1520-0426(2004)021<0777:ATFAOC>2.0.CO;2, 2004.

525 O'Neill, N. T.: Spectral discrimination of coarse and fine mode optical depth, J. Geophys. Res., 108(D17), 4559, doi:10.1029/2002JD002975, 2003.

Osborne, M., Malavelle, F. F., Adam, M., Buxmann, J., Sugier, J., Marenco, F. and Haywood, J.: Saharan dust and biomass burning aerosols during ex-hurricane Ophelia: Observations from the new UK lidar and sun-photometer network, Atmos. Chem. Phys., 19(6), 3557–3578, doi:10.5194/acp-19-3557-2019, 2019.

530 Pappalardo, G., Amodeo, A., Apituley, A., Comeron, A., Freudenthaler, V., Linné, H., Ansmann, A., Bösenberg, J., D'Amico, G., Mattis, I., Mona, L., Wandinger, U., Amiridis, V., Alados-Arboledas, L., Nicolae, D. and Wiegner, M.: EARLINET: towards an advanced sustainable European aerosol lidar network, Atmos. Meas. Tech., 7(8), 2389–2409, doi:10.5194/amt-7-2389-2014, 2014.

Pereira, S. N., Preißler, J., Guerrero-Rascado, J. L., Silva, A. M. and Wagner, F.: Forest fire smoke layers observed in the 535 free troposphere over Portugal with a multiwavelength Raman lidar: optical and microphysical properties., ScientificWorldJournal., 2014, 421838, doi:10.1155/2014/421838, 2014.

Portin, H., Mielonen, T., Leskinen, A., Arola, A., Pärjälä, E., Romakkaniemi, S., Laaksonen, A., Lehtinen, K. E. J. and Komppula, M.: Biomass burning aerosols observed in Eastern Finland during the Russian wildfires in summer 2010 - Part 1: In-situ aerosol characterization, Atmos. Environ., 47, 269–278, doi:10.1016/j.atmosenv.2011.10.067, 2012.

540 Prenni, A. J., DeMott, P. J., Sullivan, A. P., Sullivan, R. C., Kreidenweis, S. M. and Rogers, D. C.: Biomass burning as a potential source for atmospheric ice nuclei: Western wildfires and prescribed burns, Geophys. Res. Lett., 39, L11805, doi:10.1029/2012GL051915, 2012.

Randles, C. A., da Silva, A. M., Buchard, V., Colarco, P. R., Darmenov, A., Govindaraju, R., Smirnov, A., Holben, B., Ferrare, R., Hair, J., Shinozuka, Y. and Flynn, C. J.: The MERRA-2 aerosol reanalysis, 1980 onward. Part I: System 545 description and data assimilation evaluation, J. Clim., 30(17), 6823–6850, doi:10.1175/JCLI-D-16-0609.1, 2017.

Reid, J. S., Koppmann, R., Eck, T. F. and Eleuterio, D. P.: A review of biomass burning emissions part II: Intensive physical properties of biomass burning particles, Atmos. Chem. Phys., 5(3), 799–825, doi:10.5194/acp-5-799-2005, 2005a.

Reid, J. S., Eck, T. F., Christopher, S. A., Koppman, R., Dubovik, O., Eleuterio, D. P., Holben, B. N., Reid, E. A. and Zhang, J.: A review of biomass burning emissions part III: Intensive optical properties of biomass burning particles, Atmos. Chem. 550 Phys., 5(3), 827–849, doi:10.5194/acp-5-827-2005, 2005b.

Rothman, L. S., Jacquemart, D., Barbe, A., Benner, D. C., Birk, M., Brown, L. R., Carleer, M. R., Chackerian, C., Chance, K., Coudert, L. H., Dana, V., Devi, V. M., Flaud, J. M., Gamache, R. R., Goldman, A., Hartmann, J. M., Jucks, K. W., Maki,

A. G., Mandin, J. Y., Massie, S. T., Orphal, J., Perrin, A., Rinsland, C. P., Smith, M. A. H., Tennyson, J., Tolchenov, R. N., Toth, R. A., Vander Auwera, J., Varanasi, P. and Wagner, G.: The HITRAN 2004 molecular spectroscopic database, J.

555 Quant. Spectrosc. Radiat. Transf., 96(2 SPEC. ISS.), 139–204, doi:10.1016/j.jqsrt.2004.10.008, 2005.

Sakai, T., Nagai, T., Zaizen, Y. and Mano, Y.: Backscattering linear depolarization ratio measurements of mineral, sea-salt, and ammonium sulfate particles simulated in a laboratory chamber, Appl. Opt., 49(23), 4441–4449, doi:10.1364/AO.49.004441, 2010.

Schumann, U., Weinzierl, B., Reitebuch, O., Schlager, H., Minikin, A., Forster, C., Baumann, R., Sailer, T., Graf, K.,

560 Mannstein, H., Voigt, C., Rahm, S., Simmet, R., Scheibe, M., Lichtenstern, M., Stock, P., Rüba, H., Schäuble, D., Tafferner, A., Rautenhaus, M., Gerz, T., Ziereis, H., Krautstrunk, M., Mallaun, C., Gayet, J. F., Lieke, K., Kandler, K., Ebert, M., Weinbruch, S., Stohl, A., Gasteiger, J., Gro, S., Freudenthaler, V., Wiegner, M., Ansmann, A., Tesche, M., Olafsson, H. and Sturm, K.: Airborne observations of the Eyjafjalla volcano ash cloud over Europe during air space closure in April and May 2010, Atmos. Chem. Phys., 11(5), 2245–2279, doi:10.5194/acp-11-2245-2011, 2011.

565 Tesche, M., Ansmann, A., Müller, D., Althausen, D., Engelmann, R., Freudenthaler, V. and Groß, S.: Vertically resolved separation of dust and smoke over Cape Verde using multiwavelength Raman and polarization lidars during Saharan Mineral Dust Experiment 2008, J. Geophys. Res., 114, D13202, doi:10.1029/2009JD011862, 2009.

Wiegner, M. and Gasteiger, J.: Correction of water vapor absorption for aerosol remote sensing with ceilometers, Atmos. Meas. Tech., 8(9), 3971–3984, doi:10.5194/amt-8-3971-2015, 2015.

570 Wiegner, M. and Geiß, A.: Aerosol profiling with the Jenoptik ceilometer CHM15kx, Atmos. Meas. Tech., 5(8), 1953–1964, doi:10.5194/amt-5-1953-2012, 2012.

Wiegner, M., Madonna, F., Binietoglou, I., Forkel, R., Gasteiger, J., Geiß, A., Pappalardo, G., Schäfer, K. and Thomas, W.: What is the benefit of ceilometers for aerosol remote sensing? An answer from EARLINET, Atmos. Meas. Tech., 7(7), 1979–1997, doi:10.5194/amt-7-1979-2014, 2014.

575 Wotawa, G., Novelli, P. C., Trainer, M. and Granier, C.: Inter-annual variability of summertime CO concentrations in the Northern Hemisphere explained by boreal forest fires in North America and Russia, Geophys. Res. Lett., 28(24), 4575–4578, doi:10.1029/2001GL013686, 2001.

Yu, S.: Role of organic acids (formic, acetic, pyruvic and oxalic) in the formation of cloud condensation nuclei (CCN): A review, Atmos. Res., 53(4), 185–217, doi:10.1016/S0169-8095(00)00037-5, 2000.

580
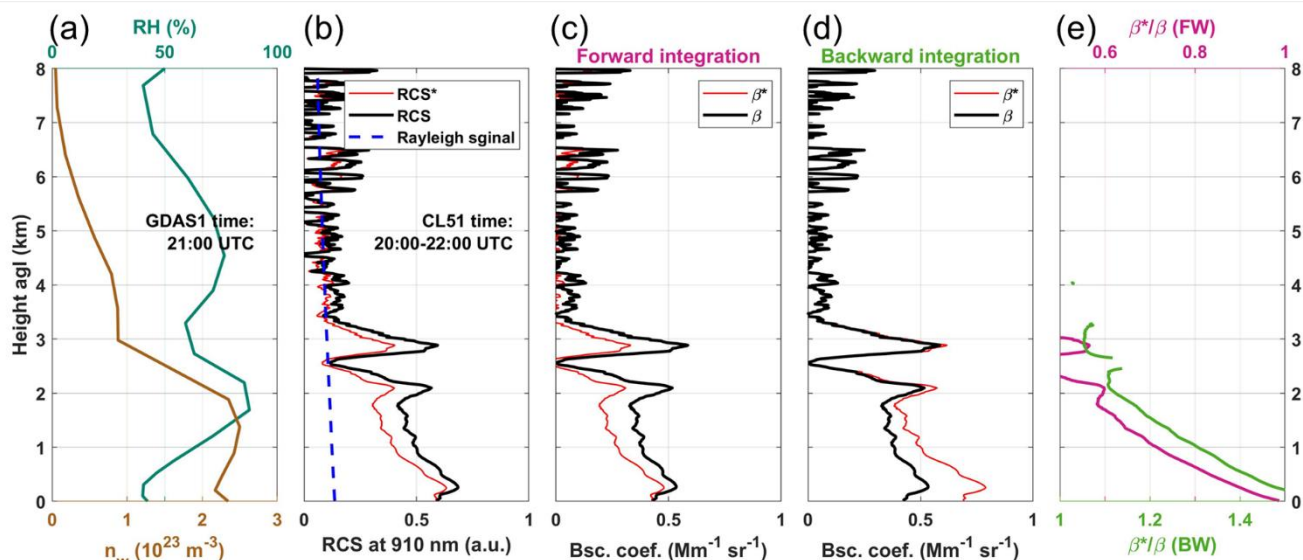
Figure 1. Example of water vapor corrections on 2 h averaged ceilometer data on 5 June 2019 (20:00–22:00 UTC). (a) Relative humidity (RH, teal) and water vapor number density (n_w, brown) from GDAS1 data at 21:00 UTC. (b) Range-corrected signal at 910 nm, without (RCS*, red) or with (RCS, black) water vapor correction, and the hypothetical Rayleigh-signal at 910 nm (dashed blue). (c) Retrieved particle backscatter coefficients: β* without (red) and β with (black) water vapor correction, using forward (FW) integration Klett solution. (d) Same as (c) but application of the backward (BW) integration. (e) Ratio of the retrieved β* and β, when using forward integration (magenta), or backward integration (green).
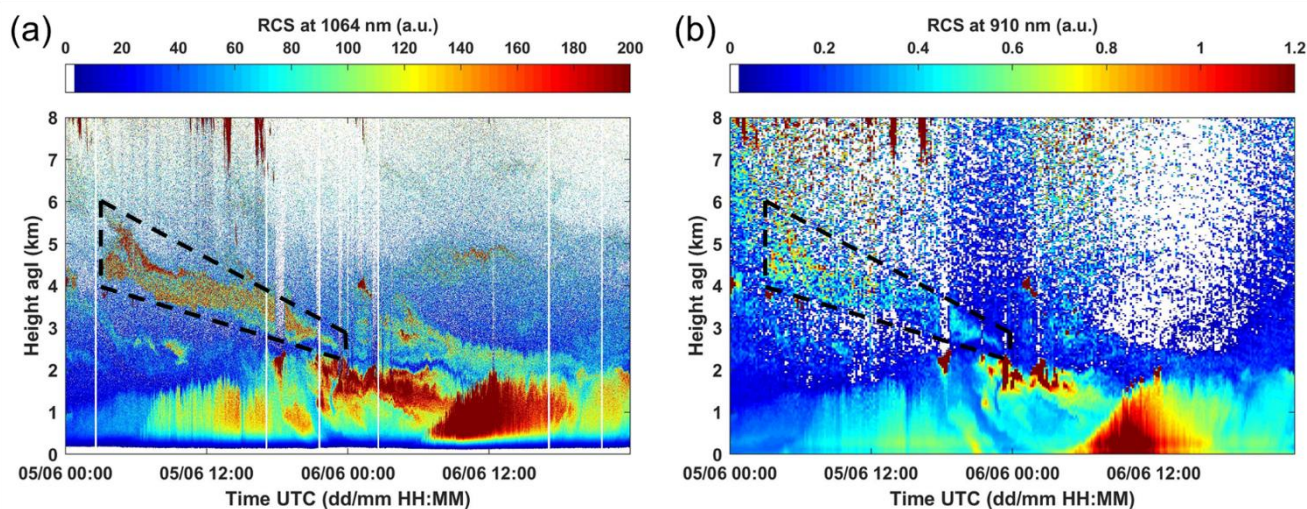
Figure 2. Time–height cross section of range-corrected signal (RCS) (a) at 1064 nm of Polly[XT], and (b) at 910 nm of CL51 ceilometer, on 5 and 6 June 2019 over Vehmasmäki station. Time is given in UTC, and height is above ground. Initial Polly[XT] data were used with temporal and vertical resolutions of 30 s and 7.5 m, respectively. CL51 data were smoothed with temporal and vertical resolutions of 10 min and 70 m, respectively. The SPoI (Smok Plume of Interest) is inside the black box with dashed lines.
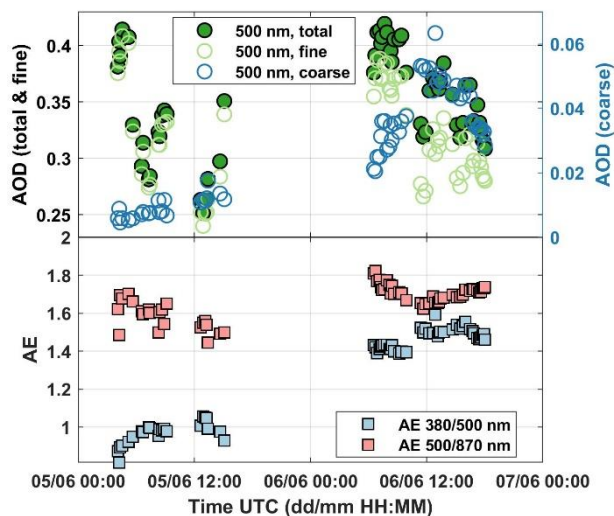
595

Figure 3. AERONET sun-photometer observations (in Kuopio station, on 5 and 6 June 2019, http://aeronet.gsfc.nasa.gov, last access: 3 May 2021) of (top) 500 nm aerosol optical depth (level 2.0 data) and (bottom) Ångström exponents (AE) computed from the optical depths measured at 380, 500, and 870 nm. The fine-mode-related (for particle with diameters < 1µm) and coarse-mode-related aerosol optical depth (diameters > 1µm) are shown in addition (top).

600
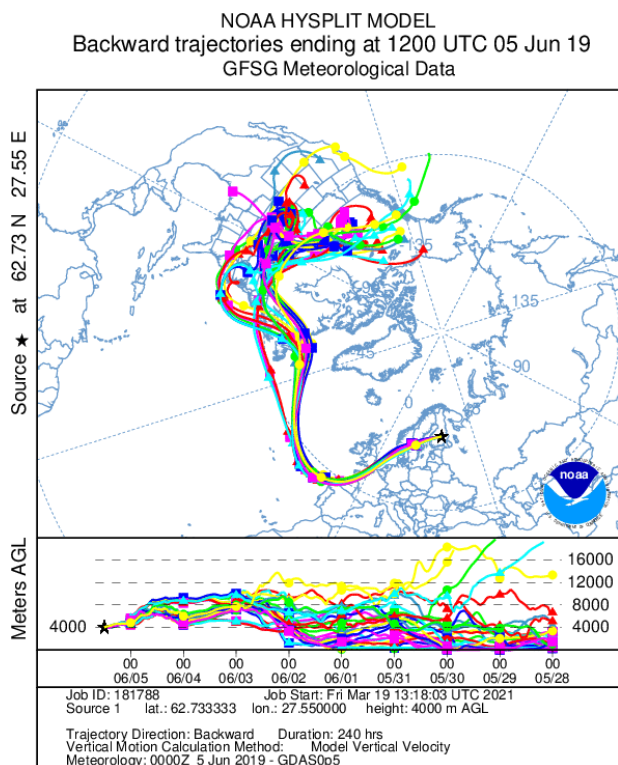
Figure 4. Ten-day backward trajectories from the HYSPLIT model (in ensemble type), ending at 12h UTC on 5 June 2019 for Kuopio, Finland. The end location of the air mass is at 4 km agl in the SPoI (Smoke Plume of Interest).
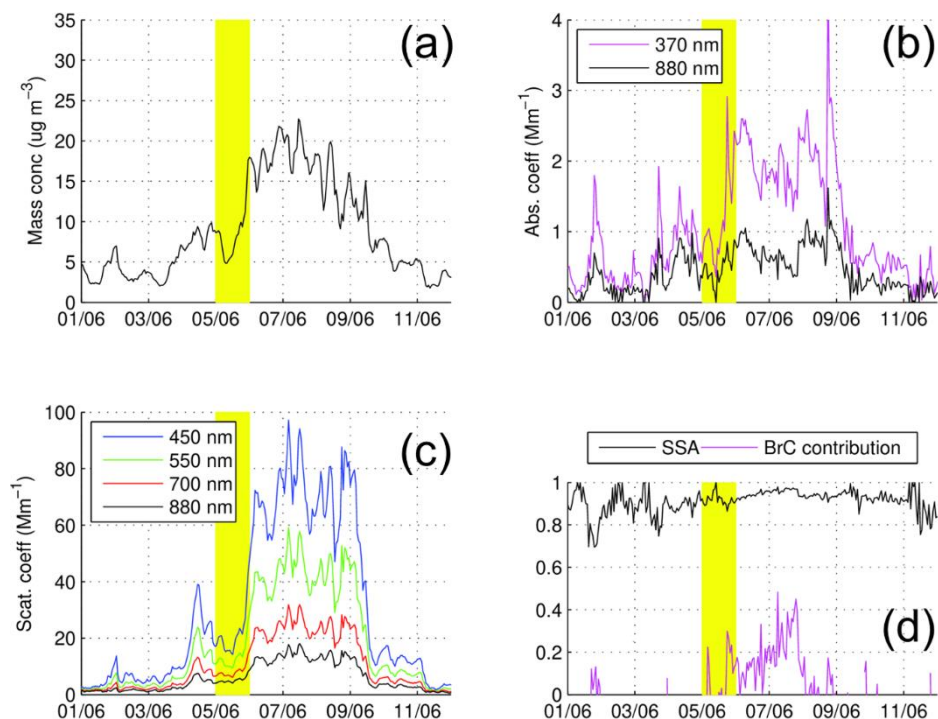
605   **Figure 5. In situ measurements of (a) mass concentrations, (b) absorption coefficients, (c) scattering coefficients, (d) single scattering albedo (SSA) at 880 nm and brown carbon (BrC) contribution, at ground level at Vehmasmäki station from 1 to 12 June in 2019. Measurements on 5 June are highlighted in yellow.**
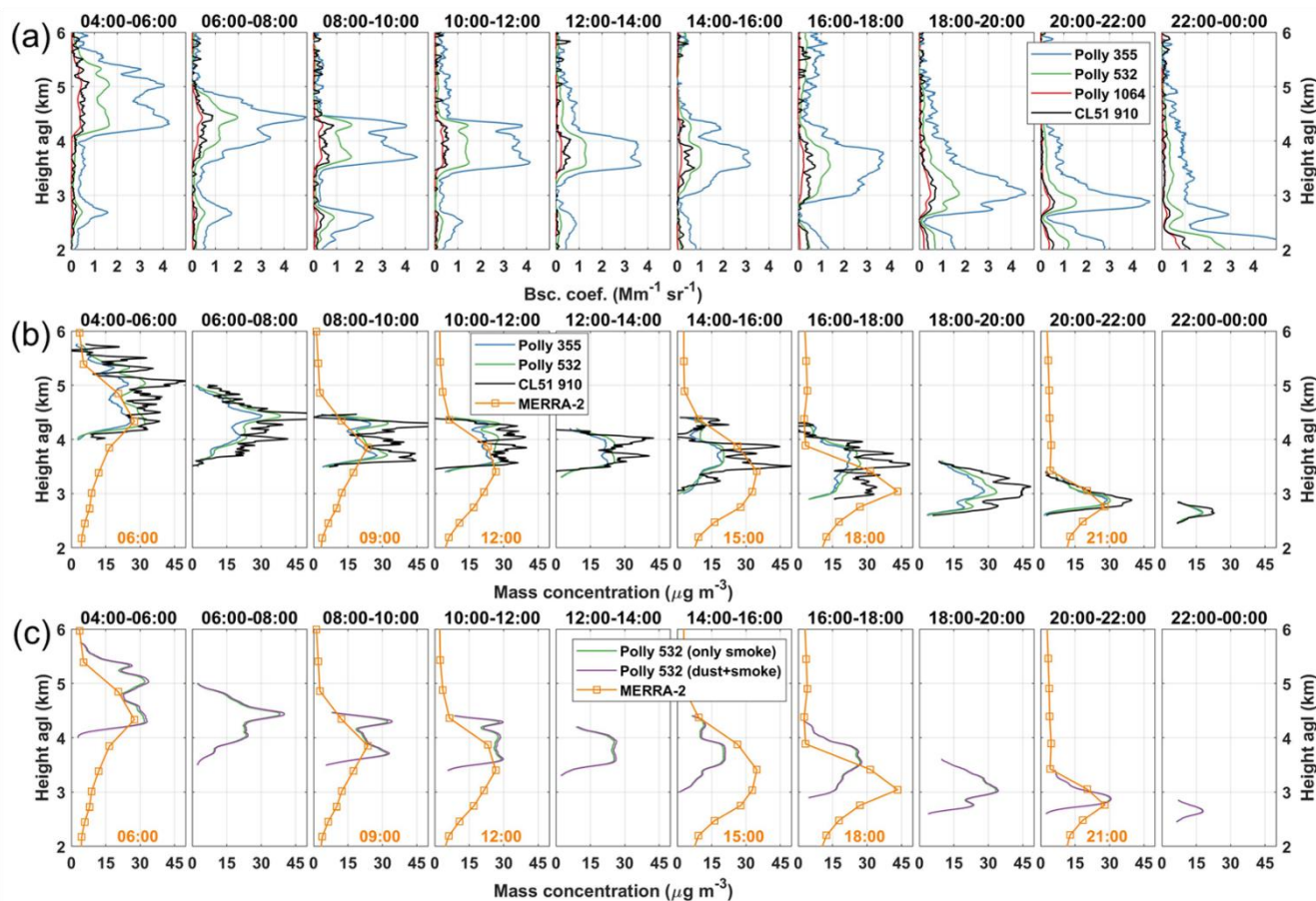
Figure 6. (a) Lidar-derived backscatter coefficients at 355 nm (blue), 532 nm (green), and 1064 nm (red) from Polly^{XT}, and at 910 nm (black) from CL51. (b) Estimated mass concentration profiles for the SPoI (Smoke Plume of Interest), based on parameters in Table 2 considering only smoke aerosols, using lidar-derived backscatter coefficients at 355 nm, 532 nm, and 910 nm. (c) Estimated mass concentration profiles, considering only smoke aerosols presence (green) or with fine dust and smoke aerosols mixture (purple) for the SPoI, using lidar-derived backscatter coefficients at 532 nm and conversion parameters in Table 3. 2 h time-averaged lidar profiles are used, with the time slot (UTC) given on top of each panel. Mass concentrations from MERRA-2 model are also shown in orange color in (b) and (c); corresponding time is given in orange color on the bottom right of each panel.
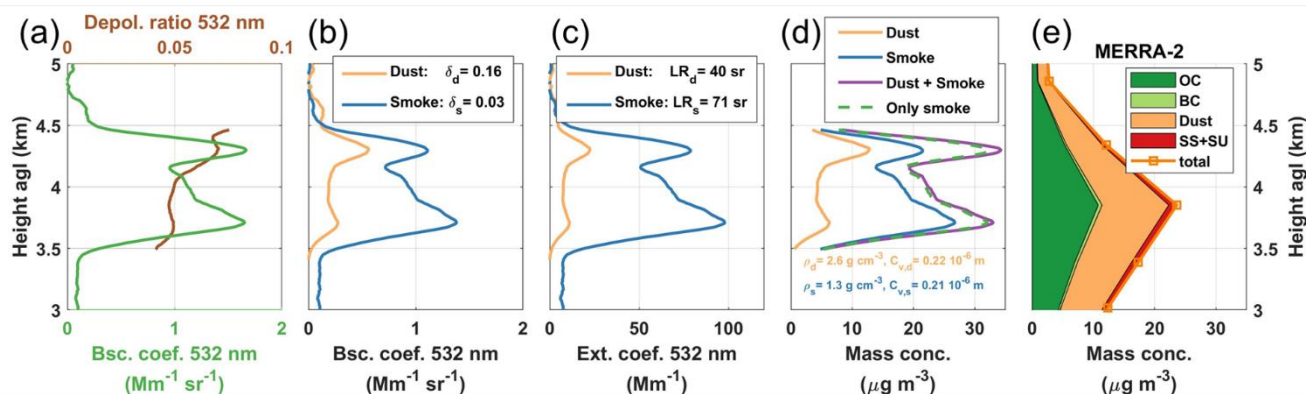
Figure 7. Lidar products obtained from Polly^{XT} measurements on 5 June 2019, 8:00–10:00 UTC (2h signal average). (a) Measured
532 nm total particle backscatter coefficient (green) and particle linear depolarization ratio (brown). (b) Particle backscatter
coefficients for fine dust (orange) and smoke (blue) particles, obtained with the POLIPHON method. (c) Respective fine dust and
smoke extinction coefficients obtained by multiplying the backscatter coefficients (in b) with the lidar ratios. (d) The fine dust
(orange), smoke (blue) particle mass concentrations derived from the extinction profiles (in c), by using parameters in Table 3. The
total mass concentrations of fine dust and smoke mixture (purple), or of only smoke particles (green) are shown. (e) Mass
concentrations of organic carbon (OC, dark green), black carbon (BC, light green), dust (orange), sea salt and sulphate (SS+SU,
red) from MERRA-2 model, at 9:00 UTC on 5 June. The total mass concentration profile is also given by orange squares.

Table 1. Optical properties (lidar ratio, particle linear depolarization ratios, backscatter- or extinction-related Ångström exponent) of biomass burning aerosols. Layer-mean values of the SPoI (Smoke Plume of Interest) are given. Optical properties found in literature of aged forest fire smoke aerosols observed in the troposphere are also given for comparisons. The source regions of these smoke aerosols are all Canada and/or Siberia.

	Lidar ratio (sr)			PDR (%)		Ångström exponent		
	355 nm	532 nm	1064 nm	355 nm	532 nm	BAE 355/532	BAE 532/1064	EAE 355/532
This study	47 ± 5	71 ± 5	-	8 ± 2	5 ± 1	2.5 ± 0.2	2.2 ± 0.3	1.4 ± 0.2
Haarig et al. (2018)	46 ± 6	67 ± 4	82 ± 22	2 ± 4	3 ± 2	2.1 ± 0.6	0.8 ± 0.3	0.9 ± 0.5
Müller et al.(2007)	46 ± 13	53 ± 11	-	-	<5	-	1.0 ± 0.4	1.0 ± 0.5
Ancellet et al. (2016)*	59 ± 5	60 ± 5	-	5 – 8	5 – 10	-	-	-
Janicka et al. (2017)	60 ± 20	100 ± 30	-	1 – 5	2 – 4	1.7 – 2.1	1.3 – 1.8	0.5 ± 0.3

* biomass burning mixing with a small amount of dust.

Table 2. Parameters required for the mass concentration retrieval.

Parameter		Value	References
Smoke mass density (g cm⁻³)		1.3	Ansmann et al. (2020)
Lidar ratio (sr)	355 nm	47 ± 5	This study
	532 nm	71 ± 5	and Haarig et al. (2018)
	910 nm*	82 ± 22	
Fine-mode volume-to-extinction conversion factor $c_{v,s}$ (10⁻⁶ m)	355 nm	0.100 ± 0.002	This study
	532 nm	0.211 ± 0.003	
	910 nm	0.620 ± 0.003	

* LR values measured at 1064 nm are used for LR at 910 nm.

Table 3. Parameters required for the mass concentration retrieval, considering fine dust and smoke mixture.

	Smoke	Fine dust
Depolarization ratio at 532 nm	0.03 (Haarig et al., 2018)	0.16 (Sakai et al., 2010)
Lidar ratio at 532 nm (sr)	71	40 (Ansmann et al., 2019)
Mass density (g cm⁻³)	1.3 (Ansmann et al., 2020)	2.6 (Ansmann et al., 2012)
Volume-to-extinction conversion factor c_v(532 nm) (10⁻⁶ m)	0.21	0.22 (Ansmann et al., 2019)